Measurement of neutral pion photoproduction off the proton with the large acceptance electromagnetic calorimeter BGOegg

N. Muramatsu,[1] J. K. Ahn,[2] W. C. Chang,[3] J. Y. Chen,[4] M. L. Chu,[3] S. Daté,[5] T. Gogami,[6] H. Goto,[7] H. Hamano,[7] T. Hashimoto,[7] Q. H. He,[8] K. Hicks,[9] T. Hiraiwa,[7] Y. Honda,[1] T. Hotta,[7] H. Ikuno,[7] Y. Inoue,[1] T. Ishikawa,[1] I. Jaegle,[10] J. M. Jo,[2] Y. Kasamatsu,[7] H. Katsuragawa,[7] S. Kido,[1] Y. Kon,[7] S. Masumoto,[11] Y. Matsumura,[7] M. Miyabe,[1] K. Mizutani,[7] T. Nakamura,[12] T. Nakano,[7] T. Nam,[7] T. N. T. Ngan,[13] M. Niiyama,[14] Y. Nozawa,[15] Y. Ohashi,[5] H. Ohnishi,[1] T. Ohta,[15] K. Ozawa,[16] C. Rangacharyulu,[17] S. Y. Ryu,[7] Y. Sada,[1] M. Sasagawa,[1] T. Shibukawa,[11] H. Shimizu,[1] R. Shirai,[1] K. Shiraishi,[1] E. A. Strokovsky,[18,7] Y. Sugaya,[7] M. Sumihama,[12,7] S. Suzuki,[5] S. Tanaka,[7] A. Tokiyasu,[1] N. Tomida,[7] Y. Tsuchikawa,[19] T. Ueda,[1] H. Yamazaki,[20] R. Yamazaki,[1] Y. Yanai,[7] T. Yorita,[7] C. Yoshida,[1] and M. Yosoi[7]

(LEPS2/BGOegg Collaboration)

[1]*Research Center for Electron Photon Science, Tohoku University, Sendai, Miyagi 982-0826, Japan*

[2]*Department of Physics, Korea University, Seoul 02841, Republic of Korea*

[3]*Institute of Physics, Academia Sinica, Taipei 11529, Taiwan*

[4]*National Synchrotron Radiation Research Center, Hsinchu 30076, Taiwan*

[5]*Japan Synchrotron Radiation Research Institute (SPring-8), Sayo, Hyogo 679-5198, Japan*

[6]*Department of Physics, Kyoto University, Kyoto 606-8502, Japan*

[7]*Research Center for Nuclear Physics, Osaka University, Ibaraki, Osaka 567-0047, Japan*

[8]*Department of Nuclear Science & Engineering, College of Material Science and Technology, Nanjing University of Aeronautics and Astronautics, Nanjing 210016, China*

[9]*Department of Physics and Astronomy, Ohio University, Athens, Ohio 45701, USA*

[10]*Department of Physics and Astronomy, University of Florida, Gainesville, Florida 32611, USA*

[11]*Department of Physics, University of Tokyo, Tokyo 113-0033, Japan*

[12]*Department of Education, Gifu University, Gifu 501-1193, Japan*

[13]*Nuclear Physics Department, University of Science, Vietnam National University, Ho Chi Minh City, Vietnam*

[14]*Department of Physics, Kyoto Sangyo University, Kyoto 603-8555, Japan*

[15]*Department of Radiology, The University of Tokyo Hospital, Tokyo 113-8655, Japan*

[16]*Institute of Particle and Nuclear Studies, High Energy Accelerator Research Organization (KEK), Tsukuba, Ibaraki 305-0801, Japan*

[17]*Department of Physics and Engineering Physics, University of Saskatchewan, Saskatoon, Canada SK S7N 5E2*

[18]*Laboratory of High Energy Physics, Joint Institute for Nuclear Research, Dubna, Moscow Region 142281, Russia*

[19]*Department of Physics, Nagoya University, Nagoya, Aichi 464-8602, Japan*

[20]*Radiation Science Center, High Energy Accelerator Research Organization (KEK), Tokai, Ibaraki 319-1195, Japan*

(Received 4 August 2019; published 8 November 2019)

Differential cross sections and photon beam asymmetries for the reaction $\gamma p \to \pi^0 p$ have been measured in the photon beam energy range of 1.3–2.4 GeV and the π^0 polar angle range of $-1 < \cos\theta^{\mathrm{c.m.}}_{\pi^0} < 0.7$. The measurement has been done by using a large acceptance electromagnetic calorimeter in the SPring-8 LEPS2/BGOegg experiment. The results of the photon beam asymmetry in a wide π^0 polar angle range are new for the photon beam energies exceeding 1.9 GeV. None of the existing partial wave analysis models describe the observed asymmetries in the high energy region. The contribution of multipole amplitudes with an orbital angular momentum of 5 in the πN system has been found to be important at these energies.

DOI: 10.1103/PhysRevC.100.055202

I. INTRODUCTION

The spectroscopy of baryon resonances has provided essential information on the internal composition of hadrons. The ground and excited states of baryons consisting of nonstrange quarks have been intensively studied by pion-nucleon scattering experiments and meson electro- or photoproduction off the nucleon [1]. The experimentally identified mass and properties of lower mass states have been consistently explained by the constituent quark models with the spin-flavor SU(6) symmetry for light quarks [2]. In contrast, the predictions by these models do not fully reproduce the observed masses of higher excited states. Moreover, some of the predicted states are missing from experimental analyses. These facts may suggest the possibility of rich structures for baryons beyond the existing constituent quark models. Therefore, it is natural to further clarify the spectrum of excited baryons with improved experimental measurements.

In order to establish the baryon mass spectrum including the highly excited states, π^0 photoproduction off the proton

has been studied by many experiments as one of the fundamental measurements with moderately high statistics. Differential cross sections and spin observables have been measured so far at CEA [3], Yerevan [4], Daresbury [5,6], MAMI [7,8], GRAAL [9], CB-ELSA [10–14], CLAS [15,16], and SPring-8/LEPS [17]. Because the π^0 meson is an isotriplet, the s-channel diagram couples to the excited states of both the nucleon (N^*) and the Δ (Δ^*). From past measurements, the importance of the $N(1520)D_{13}$ and the $N(1535)S_{11}$ resonances, as well as $N(1680)F_{15}$ and $\Delta(1700)D_{33}$, have been known in the so-called second and third resonance regions, respectively. Although many results have been available for this reaction, there are still small discrepancies in the differential cross sections measured by different experiments, for example, at the most backward π^0 angles and the photon beam energies around $1.2 < E_\gamma < 1.9$ GeV, as discussed later. Such difference affects the results of partial wave analyses (PWA) in terms of the introduction of new resonances and the precise determination of resonance contributions. The present work provides additional experimental information for the differential cross sections.

In photoproduction experiments, photon beam asymmetry is a useful tool to decompose the overlapping baryon resonances. Photon beam asymmetry is defined by the degree of asymmetry in the π^0 azimuthal angle distribution relative to the linear polarization vector of a photon beam. In PWA model calculations, it is expressed by the helicity amplitudes with interference, which can possibly enhance small contributions from higher multipoles [18]. Even for π^0 photoproduction, the measurements of photon beam asymmetry are still scarce in the high energy region, where the polarized photon beam is usually produced by means of coherent bremsstrahlung radiation with a low degree of polarization. This article presents the results of the first-time measurement of the photon beam asymmetries for a wide range of π^0 polar angles, $-1 < \cos\theta^{\rm c.m.}_{\pi^0} < 0.6$, with $E_\gamma > 1.9$ GeV by using a photon beam originating from laser Compton scattering. Our measurement of the photon beam asymmetries together with the differential cross sections shall help to differentiate baryon resonances.

This article is organized in the following manner. Section II describes the photon beam properties, the experimental setup of detectors, and the collected data along with luminosity evaluation. Section III explains the analysis method including event reconstruction, the event selection, and the kinematic fit. The description of the selected sample is given at the end of Sec. III. The measured differential cross sections and photon beam asymmetries are shown together with the existing results of other experiments in Sec. IV. The comparison of the experimental results with PWA model calculations is discussed in Sec. V. The summary of this article follows in Sec. VI.

II. EXPERIMENT

A. Photon beam

The BGOegg experiment has been carried out at SPring-8 BL31LEP, called the LEPS2 beamline. The data set for the present analysis was collected from Nov. 2014 to Feb. 2015. At the LEPS2 beamline, the photon beam is produced by the backward Compton scattering of 355 nm ultraviolet laser light from 8 GeV electrons in the storage ring [19]. The maximum energy that the photon beam reaches is 2.4 GeV at the Compton edge.

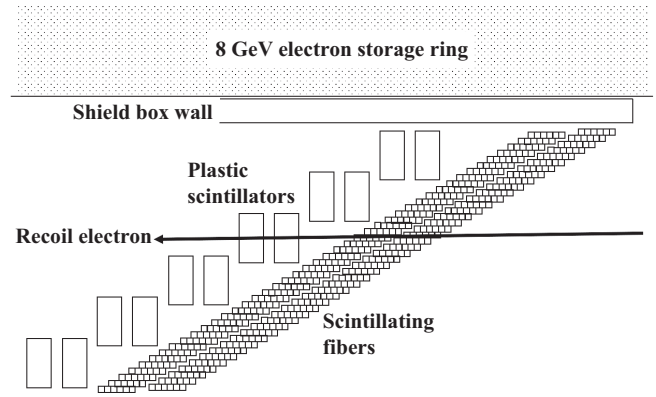

FIG. 1. Schematic view of the tagging detector. Only the part near the storage ring is shown.

The photon beam energy was measured for every event by tagging a recoil electron from the laser Compton scattering. As shown in Fig. 1, a tagging detector with two layers of 1 mm-squared scintillating fiber bundles is placed at the downstream exit of a bending magnet in the storage ring. The momentum of the recoil electron was analyzed as a function of the fiber hit position. The photon beam energy was then obtained from the energy conservation in the laser Compton scattering. The photons above 1.3 GeV are tagged at the LEPS2 beamline. The photon beam intensity was also measured at the tagging detector by counting the trigger signals of recoil electrons. For making the trigger signals, an additional two layers of 8 mm-wide plastic scintillators are included, as shown in Fig. 1. The tagged beam intensity was typically $1–1.5 \times 10^6$ photons/s during the collection of the data presented here.

The photon beam from laser Compton scattering has a great advantage of high linear polarization, whose degree can be calculated by Eq. (16) of Ref. [20]. At the Compton edge of the LEPS2 case, the degree of polarization reaches a maximum of 94% by transferring the linear polarization of the laser light. This feature is highly attractive for measuring the spin observables associated with linear polarization in hadron photoproduction reactions.

The photon beam is delivered from the Compton scattering point to the BGOegg experimental setup, located 125 m downstream. The BGOegg experimental setup is assembled inside the LEPS2 experimental building, which has been newly constructed outside of the storage ring building. A long vacuum pipe is employed for the photon beam path between the storage ring and the LEPS2 experimental building. Some of the photons are lost during the beam transfer due to thin vacuum windows, made of an aluminum plate and polymer films, and an x-ray absorber of a 1 mm-thick tungsten plate. Electron and positron pairs created at the tungsten absorber are swept by a magnet inside the storage ring tunnel. The transmission factor of the photon beam reaching the detector

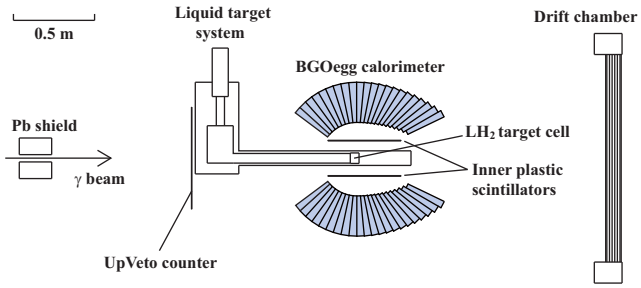

FIG. 2. Setup of the BGOegg experiment. Only the apparatus closely related to the signal selection is shown in a side view.

system of the BGOegg experiment is estimated to be 77.2% by a simulation based on GEANT4 [21].

In the most upstream part of the LEPS2 experimental building, a buffer shield with a 45 mm-diameter hole has been constructed using lead blocks to minimize accidental particles entering into the BGOegg calorimeter, described in the next subsection. In the space between the buffer shield and the BGOegg experimental setup, a large plastic scintillator is placed to remove the contamination of charged particles in the photon beam. This scintillator is called the UpVeto counter. Its size is 620×620 mm^2, which is large enough to also reject charged particles from upstream hitting the BGOegg calorimeter directly.

B. BGOegg experimental setup

Figure 2 shows the detector setup of the BGOegg experiment. At the origin of the detector coordinate, a liquid hydrogen target (LH_2) was placed to be irradiated by the photon beam. The target cell is made of thin polyimide films and is formed in a cylindrical shape, 54 mm long with a diameter of 65 mm. The target is mounted on the top of a 760 mm-long copper pipe, through which the photon beam can pass. Buffer tanks for about 300 L of hydrogen gas are connected with the target cell through a refrigerator system. A part of the hydrogen gas inside this closed system was liquefied in the refrigerator reservoir and the target cell by lowering the cooling temperature to about 20 K. The long pipe of the target system is covered by a cylindrical vacuum chamber, made of 1 mm-thick carbon-fiber-reinforced plastic (CFRP).

The liquid hydrogen target is surrounded by a large-acceptance electromagnetic calorimeter, called "BGOegg". This is the major detector for photoproduced particles in the BGOegg experiment. The BGOegg calorimeter consists of 1,320 $Bi_4Ge_3O_{12}$ (BGO) crystals, which are put together in the shape of an "egg". Individual crystals have 20 radiation lengths in depth, and cover 6° in the azimuthal direction to form a ring of 60 crystals. These rings are stacked into the forward 13 and backward nine layers, corresponding to a polar angle range from 24° to 144°. There is no supporting materials between the BGO crystals. The egg-shape is maintained by tightening truncated square pyramidal crystals from the outside egg-surface and the two end-cone plates.

The light output of each BGO crystal was read by a bialkali photomultiplier tube (PMT). The analog signal of the PMT output was recorded by 11-bit FERA ADCs for the charge (energy) measurement, while its discriminated signal was used for the trigger logic and the timing measurement with TDCs having 100 ps timing resolution. The energy calibration for individual crystals were performed such that, after an iteration process, the invariant mass of two γ's, whose energy was mainly deposited into the crystal being calibrated, should be peaked at the nominal value of the π^0 mass [22]. The temperature dependence of the crystal light yield and the PMT response has been known to be a rate of about -1.5%/K in total. Therefore, the BGOegg calorimeter and the associated detectors, described below, are set up inside a thermostatic booth to maintain the temperature within ± 1 °C.

The energy resolution of the BGOegg calorimeter has been estimated to be 1.3% at the incident energy of 1 GeV by a test experiment using a prototype detector [23]. In addition, the high granularity of the calorimeter allows a good precision determination of the γ direction. The π^0 mass resolution in the $\gamma\gamma$ decay mode is about 6.7 MeV/c^2 with a 20 mm-thick carbon target, indicating the world highest performance in this energy region. The observed mass resolution is consistent with the simulation result which was obtained by inputting the γ energy resolution from the prototype test.

In addition to photons, charged particles were detected in the BGOegg calorimeter. The charge identification of the detected particles was done by the inner plastic scintillators (IPS), which are installed inside the calorimeter by placing 30 slats of 453 mm-long and 5 mm-thick scintillators side by side in a cylindrical shape. The energy deposit signal of a charged particle was read out by multipixel photon counters (MPPC) from the upstream end of individual IPS slats. The timing and energy of signals were calibrated depending on the BGOegg layer number (or the polar angle) of the charged particle hit.

The forward region, with polar angles less than 22°, was covered by a planar drift chamber (DC), which detected charged particles in the acceptance hole of the BGOegg calorimeter. The DC has six layers of 80 sense wires, whose interval is 16 mm. Squared drift cells are formed by potential wires at the middle positions of the sense wires and the aluminized mylar cathode films at the planes 8 mm apart from the wire planes. The directions of sense wires in each of two layers are arranged in three azimuthal angles with a relative difference of 60°. Thus, the DC has a hexagonal shape, whose sensitive area mainly corresponds to an inscribed circle with a diameter of 1280 mm. It was installed 1.5 m downstream of the target. The position resolution at the individual drift planes was typically 300 μm.

At a distance of 12.5 m downstream of the target, we put a time-of-flight counter wall of resistive plate chambers (RPC), covering the polar angle region less than 7°. The RPC has a good time resolution of 60–90 ps, which provides a proton momentum resolution of about 1% at 2 GeV/c. The present analysis does not use the RPC explicitly, but it has been employed for data calibration, efficiency evaluation, and so on.

C. Collected data

The minimum-bias trigger logic was generated by the coincidence of a recoil electron hit at the tagging detector and photoproduced particle hits at two or more BGO crystals. The trigger signal at the tagging detector was made by the simultaneous hits of the two-layer trigger scintillators, which were geometrically overlapped in the path of a recoil electron. While the trigger inefficiency coming from the calorimeter side is negligible for the present analysis, the tagging detector trigger has a large dead time because of the high beam rate, as discussed below. The trigger rate was typically 200–300 events/s, resulting in the data acquisition (DAQ) efficiency of about 95%.

The integrated number of beam photons in the tagged energy range was obtained by summing up the scaler counts of the tagging detector trigger during the experimental period. The storage ring electrons are localized by various patterns of bunch filling with 508 MHz radio frequency (RF) [24], so that a large inefficiency of the tagging detector trigger, whose logic signal width is 20 ns, is easily caused by simultaneous or continuous laser Compton scatterings, depending on the electron filling pattern and the photon beam intensity. Since the amount of this dead time is governed by a purely statistical phenomenon, we have evaluated the correction factor for the measured trigger counts at the tagging detector by using a Monte Carlo (MC) simulation. After applying the correction factor, the total counts of the tagging detector trigger $N_{\rm tag}^{\rm corr}$ reach 3.586×10^{12} for the present data set.

There is a wall structure between the tagging detector scintillators and the electron storage ring. A part of the recoil electrons with high momenta hit this wall, generating an electromagnetic shower, which produces a fake trigger signal at the tagging detector. The shower contamination rate $f_{\rm shower}$ in the tagging detector triggers was estimated to be 4.2% from a special run taken with a lead glass calorimeter on the photon beam. This special run was collected by employing only the tagging detector trigger, to measure the photon beam energy spectrum and distinguish its shower component, which was localized around 1.1 GeV.

The total number of incident photons on the liquid hydrogen target was obtained by multiplying the transmission factor of the 125 m-long beamline $T_{\rm sim}$ (77.2%) and the tagging detector trigger counts $N_{\rm tag}^{\rm corr}$. The photon beam transmission factor was further corrected with an additional multiplication factor $T_{\rm corr}(E_\gamma)$ depending on the photon beam energy E_γ in MeV:

$$T_{\rm corr}(E_\gamma) = 1 + 1.206 \times 10^{-5}(2300 - E_\gamma) - 1.113 \times 10^{-7}(2300 - E_\gamma)^2. \quad (1)$$

This correction is necessary due to a 7 mm-diameter collimator, placed upstream of the LEPS2 beamline. The reduction of photons is caused by a slight shift of the beam path at the laser focus optimization. Equation (1) was evaluated by fitting a second-order polynomial function to the energy-dependent ratio of π^0 yields and tagging detector counts ($R^i_{\pi^0/tag}$), which were normalized in each photon beam energy bin i by using the period with good beam position. The lower energy region is more influenced because the photon beam size (or the cone angle of the scattered photons) becomes larger by the kinematics of laser Compton scattering. No clear evidence of beam loss was observed at higher energies, so that a common scale factor for all $R^i_{\pi^0/tag}$ was further adjusted by forcing $R^{i^{\rm max}}_{\pi^0/tag}$ to 1 in the highest beam energy bin $i^{\rm max}$, before the fit of Eq. (1).

The luminosity $\mathcal{L}$ of the collected data was finally evaluated by multiplying the incident number of photons and the number of protons in the liquid hydrogen target with the thickness $d_{\rm target}$ of 54 mm:

$$\mathcal{L} = N_{\rm tag}^{\rm corr}(1 - f_{\rm shower})T_{\rm sim}T_{\rm corr}^{\rm ave}N_{\rm Avo}\rho_{\rm target}d_{\rm target}. \quad (2)$$

Here, $T_{\rm corr}^{\rm ave}$ represents the weighted average of $T_{\rm corr}(E_\gamma)$ for the photon beam energy range, which is subject to the measurement of the luminosity. Avogadro's constant and the density of liquid hydrogen (0.0708 g/cm^3) are expressed by $N_{\rm Avo}$ and $\rho_{\rm target}$, respectively. The obtained luminosity was used for the calculation of the differential cross sections.

The energy-dependent transmission factor $T_{\rm corr}(E_\gamma)$ was confirmed by collecting the e^+e^- conversion events, created at the liquid hydrogen target. The e^+e^- tracks were detected at the central region of the DC. The number of beam photons at the target was deduced from the well-known pair creation cross section, available by the NIST XCOM database [25]. The energy-dependent ratio of the estimated number of photons and the trigger counts at the tagging detector was found to be consistent with Eq. (1) within a few % difference at most. This difference was taken into account at the estimation of systematic errors.

III. DATA ANALYSIS

A. Event reconstruction

The photon beam energy was measured event by event from the hit position of a recoil electron at the tagging detector. For this measurement, a recoil electron track was offline reconstructed by connecting two-layer fiber hits and two-layer trigger scintillator hits geometrically and by requiring timing consistency of the trigger scintillator hits. Since the different layers of 1 mm-wide fibers are shifted by their half size, the track position can be measured at each 0.5 mm step. This precision was found to be sufficient when compared with the hit position spread expected from the electron beam divergence, whose influence dominates the photon energy resolution.

The photon beam energy calibration at the tagging detector was done by predicting the true value without using the recoil electron hit position. In one way, the photon energy was predicted by treating it as an unmeasured variable in the kinematic fit of the reaction $\gamma p \to \pi^0\pi^0 p$, whose final state particles were all detected in the BGOegg calorimeter. In another method, the momentum of an extremely forward proton was measured by the RPC in order to predict the photon energy from the missing mass of the reaction $\gamma p \to Xp$, where X was a π^0 or η meson. The predicted energies were plotted as a function of the hit position at the tagging detector for fitting a fourth-order polynomial function. The

two calibration results were averaged with the weights of their precisions.

The photon beam energy resolution was estimated to be 12 MeV by comparing the photon energy obtained from the tagging detector and the value predicted from a kinematic fit. The kinematic fit was performed by using an independent sample of the reaction $\gamma p \to \pi^0 \eta p$ with a forward proton detection at the RPC. The estimated resolution was confirmed by an alternative method, where an error function was fitted to the Compton edge for extracting a smeared resolution. The resolution value of 12 MeV is consistent with the naive expectation from the electron beam divergence and the tagging detector geometry.

The Moliere radius inside BGO is 22.3 mm, whereas the inner profile of each BGO crystal is a trapezoid with the side lengths of about 20 mm. Therefore, the electromagnetic shower of a γ deposits its energy into about ten to a few tens of neighboring crystals in the BGOegg calorimeter. A "cluster" of such an electromagnetic shower was reconstructed by connecting the neighboring crystals whose energy was greater than the discriminator threshold of about 10 MeV. Then, peripheral crystals with smaller energies were added to the central crystals. The energies of all cluster members were summed up to measure the energy of a γ. If a small-energy crystal, which had no TDC hit, was shared by different clusters, then its energy was divided with the energy ratio of the relevant clusters. The direction of the detected γ was decided by the straight line from the target center to the core crystal, whose energy deposit was largest among the cluster members.

During the electromagnetic shower evolution, small sub-clusters can be produced in association with a main γ cluster. Such a sub-cluster is called a "leak cluster". The energy of the leak cluster ($E_{\rm leak}$) was added to that of the nearest main γ cluster ($E_{\rm main}$) if there were leak clusters within 120 mm of the main cluster under the conditions of $E_{\rm leak}/E_{\rm main} < 0.07$ and $R > 180 E_{\rm leak}/E_{\rm main} - 2.0$. Here, the variable R is defined as the energy-weighted average of the distances from the cluster center to the cluster members, indicating the effective cluster size. These conditions have been obtained on the basis of a detail analysis for γ clusters in both MC and real data, and represent that the leak cluster tends to have a small energy and a different shape compared with the usual γ cluster. The energy correction by leak clusters recovers the 2γ invariant mass peak to the nominal value of the π^0 mass. Moreover, the acceptance loss due to rejecting background-like events with three or more neutral clusters is avoided.

In the present analysis, the DC, having zero magnetic field, measures only the direction of an outgoing proton. It also vetoes extra charged tracks, which likely originate from background processes. A straight line was fitted to each event with four or more layer hits, and the fit was repeated while removing outliers until the χ^2 probability was reasonable. The efficiency of finding a DC track, including both detection and reconstruction efficiencies, was estimated to be 0.982 ± 0.004 by analyzing photoproduction reactions with a forward proton detected independently at the RPC. The tracks with a χ^2 probability greater than 1% were accepted for the further analysis.

B. Event selection

In the present analysis, the $\gamma p \to \pi^0 p$ events were extracted from the data taken with the liquid hydrogen target, as described in Sec. II C. The π^0 meson was detected by the BGOegg calorimeter in the decay mode into $\gamma\gamma$, whose branching fraction is 0.98823 ± 0.00034. A combination of two neutral clusters was searched for by restricting the time difference of the core crystals within 10 ns. Individual cluster energies were required to be greater than 30 MeV. If the core crystal of either neutral cluster was found in the most forward or backward BGOegg layer, such an event was removed from the analysis sample in order to avoid the insufficient energy measurement due to the electromagnetic shower leak at the outside of the calorimeter. The effective cluster size R was required to be less than 20 mm so that overlapped showers should not be identified as one cluster.

The energies of the two neutral clusters were corrected by adding the leak cluster energies, as mentioned in Sec. III A. Then, the existence of additional neutral clusters was examined at the reaction time. Events with three or more neutral clusters were rejected as backgrounds, mainly coming from multiple pion photoproduction.

In addition to the two neutral clusters, a proton was simultaneously detected by either the BGOegg calorimeter or the DC. In the BGOegg calorimeter, a cluster signal due to the energy loss of the proton was searched for within the time range of -5 to 20 ns of the reaction time to accept a low momentum proton. A charge of the cluster was identified by examining an IPS hit on the line between the target and the BGOegg cluster center. As for the proton detection at the DC, the number of reconstructed tracks was counted without a timing requirement. It was confirmed that the straight track passed through the target region geometrically.

The total number of charged particles at the BGOegg calorimeter and the DC was limited to one by assuming this hit arose from an outgoing proton. However, there exists a possibility of accidental DC hits due to e^+e^- pair creation by the beam photons originating from a different electron bunch because the DC hit timing cannot be recognized precisely. Therefore, if a proton was detected in the BGOegg calorimeter, extra DC tracks were accepted at the central part of the DC, defined by the 30 mm-squared region around the beam axis. In addition, a proton flying into the boundary region of the BGOegg calorimeter and the DC tends to leave hit signals in both of these detectors by producing DC tracks due to an interaction at the BGO crystals. Such events were accepted if $\sin\alpha < 0.26$ was satisfied, where α denotes the opening angle between the BGOegg and DC tracks. This condition increases the acceptance and reduces the systematic uncertainty.

The number of reconstructed tracks at the tagging detector was required to be one per event to avoid the ambiguity in measuring the photon energy. However, events with two or more recoil electron tracks were accepted if only one track was identified at the timing of the π^0 photoproduction reaction. The reaction timing was determined by an accelerator RF signal, which was recorded to the data only with a several ps jitter. Since the RF signals were distributed with about 2 ns intervals, the correct electron bunch was chosen on the basis of

the BGOegg γ cluster timing in the case of multiple tagging detector tracks. By introducing a condition to recover such multi-track events, the size of the selected π^0 photoproduction sample increases by 7.5%.

It was also confirmed that there was no hit at the UpVeto counter within $\pm 3\sigma$ of the reaction time window.

C. Kinematic fit

For the final event selection, a kinematic fit was performed to identify the topology of the reaction $\gamma p \to \pi^0 p \to \gamma\gamma p$. The proton momentum in the final state was treated as an unmeasured variable, whereas ten quantities including the energies of two γ's, the polar and azimuthal angles of those γ's and of a proton, the position of a reaction vertex along the beam axis, and the photon beam energy were varied based on pre-estimated resolutions. The variables for the polar and azimuthal angles, θ and ϕ, were replaced to the form of $r \cdot \theta$ and $r \cdot \sin\theta \cdot \phi$, respectively, with the distance r from the target center to the BGOegg cluster core. This representation was adopted for an unbiased fit, to minimize the variation of the estimated resolutions that depend on the polar angle θ.

A realistic simulation was made with the BGOegg experimental condition, to obtain the resolutions of the energies and directions for reaction products. These resolutions were evaluated as a function of the polar angle, which was correlated with the effective thickness of detector materials, the reaction vertex ambiguity due to the target length and the photon beam size, the typical momentum value of photoproduced particles, and so on. The γ energy resolution is also dependent on the cluster energy itself. Small correction factors to the simulated resolutions were further applied after inspection of the pull distributions in the real data. The validity of the predetermined resolutions was confirmed by the flatness of the χ^2 probability distribution in the kinematic fit.

In the kinematic fit of the present analysis, we constrained the invariant mass of the two γ's to be the nominal value of the π^0 meson mass. The four-momentum conservation between the initial and final states was also required as the constraint conditions. If the χ^2 probability exceeded 2%, those events were accepted as the signals of π^0 photoproduction off the proton.

D. Selected sample

Finally, 647 058 events were selected to obtain the differential cross sections. Figure 3 shows the $\gamma\gamma$ invariant mass distribution of the selected signal sample. Here the measured energy and direction of γ's are used for the invariant mass calculation. The signal events are well peaked at the nominal π^0 mass with a resolution σ of about 8 MeV/c^2.

As seen in Fig. 3, no irregular components of backgrounds are observed in the invariant mass spectrum. Nevertheless, there is the possibility of background contamination in the π^0 mass peak region after the kinematic fit. Such a background can arise only from the reaction $\gamma p \to \pi^0\pi^0 p$ with missing γ's, in view of its large cross section and the geometrical acceptance of the BGOegg calorimeter. In order to estimate the background contamination, an independent sample with a full detection of the final state particles in the reaction

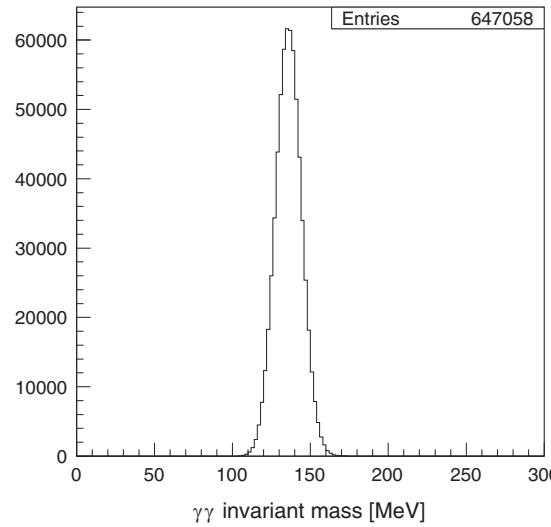

FIG. 3. Distribution of the $\gamma\gamma$ invariant mass in the final signal sample.

$\gamma p \to \pi^0\pi^0 p \to \gamma\gamma\gamma\gamma p$ was selected from the collected data. The resonance contributions in the $\pi^0 p$ system, coming from Δ^+, $N(1520)^+$, etc., were observed in addition to the non-resonant $\pi^0\pi^0 p$ final state. The template spectra of the $\pi^0 p$ invariant mass were generated by the MC simulations of the background processes, and they were fitted to the real data spectrum at several beam energy slices in order to determine the normalization factors individually. Then, the 2γ detection analysis, using the normalized MC samples, was done in the same way as that for the the reaction $\gamma p \to \pi^0 p$, to evaluate the background contamination ratio depending on the photon beam energy and the π^0 polar angle. The contamination ratio turned out to be small, with typical values of 0.1–0.2 %, while its slight rises to about 0.8% were seen at the highest photon beam energies.

We have also collected the data with an empty target, where the target cell is filled by gasified hydrogen. In this case, the amount of materials irradiated with the photon beam is dominated by the cell films. Therefore, a background contamination from the cell films in the π^0 photoproduction yield was estimated by analyzing this empty target data with the same event selection conditions as those in the liquid hydrogen data analysis. After normalizing the sizes of the empty and liquid hydrogen target data by using the integrated numbers of tagging detector triggers, the contribution from the cell films was found to be less than 0.2% at most of the photon beam energies and π^0 polar angles. Slight increases up to 0.8% were observed at the most backward angles. As the results of inspections for the reaction $\gamma p \to \pi^0\pi^0 p$ and the target cell film contribution, those background contaminations were neglected in the present analysis.

IV. RESULTS

A. Differential cross section

The yields of the reaction $\gamma p \to \pi^0 p$ were obtained in 22 photon beam energy bins for $1300 < E_\gamma < 2400$ MeV

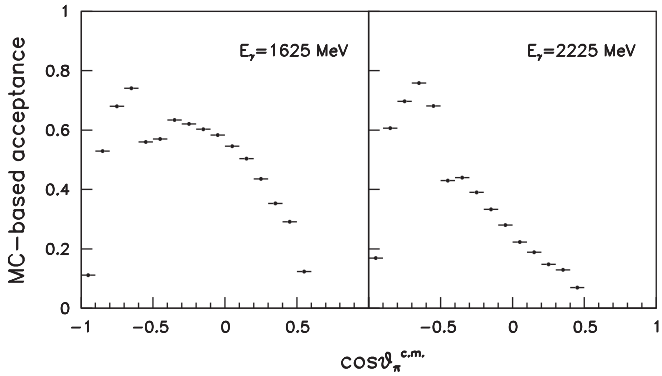

FIG. 4. Acceptance factors obtained by GEANT4-based MC simulation with the realistic detector setup. Two 50 MeV-bins, corresponding to the photon beam energies of 1625 and 2225 MeV, are shown as examples.

and 17 π^0 polar angle bins for $-1.0 < \cos\theta^{\rm c.m.}_{\pi^0} < 0.7$. In these kinematical bins, the number of remaining events were counted after the event selection described in the previous section. The background contamination was neglected as explained.

The geometrical acceptance factors including the influence of the physics processes like the e^+e^- conversions of γ's, the shower evolution in the detector materials, the ionization energy loss of charged particles, etc., were evaluated by the GEANT4-based MC simulation with the precise detector geometry of the BGOegg experiment. The energy and polar angle distributions inside the finite sizes of the individual kinematical bins have non-negligible effects in the acceptance evaluation, so that the MC simulation sample must be generated with realistic kinematical distributions. Accordingly, the MC-based acceptance evaluation was iterated by reflecting the measured differential cross sections at the previous step to the kinematical distributions of the next-step MC sample. This iteration was repeated until the acceptance change came to converge within 1%. The acceptance factors of two energy bins are shown in Fig. 4, as examples. The dip structure at $\cos\theta^{\rm c.m.}_{\pi^0} \approx -0.5$ can be understood as a boundary effect of the BGOegg calorimeter and the DC in the detection of protons. There is no acceptance in the most forward region due to the limited calorimeter coverage.

The total luminosity in the tagged energy range, described in Sec. II C, was divided into the photon energy bins of 50 MeV for use in the construction of differential cross sections. The luminosities at the individual energy bins were evaluated from the intensity fractions in the calculated energy spectrum of laser Compton scattering. Eq. (8) of Ref. [20] was adopted as the differential cross section of laser Compton scattering to obtain the energy spectrum. In addition, the photon beam transmission factor at each energy bin was calculated from the energy dependence determined in Eq. (1). The energy-binned luminosity was used for all of the π^0 polar angle bins in the calculation of the π^0 photoproduction cross sections.

The differential cross section $d\sigma/d\Omega$ of the reaction $\gamma p \to \pi^0 p$ was calculated at each kinematical bin i of the photon beam energy and the π^0 polar angle:

$$\left(\frac{d\sigma}{d\Omega}\right)^i = \frac{N^i_{\pi^0}\, F^i_{\rm bin}\, F^i_{\rm conv}}{A^i_{MC}\, Br\, \epsilon^i_{\rm proton}\, \epsilon^i_{\rm tag}\, \mathcal{L}^i\, \Omega^i}, \tag{3}$$

where $N^i_{\pi^0}$, A^i_{MC}, $\mathcal{L}^i$, and Ω^i are the π^0 photoproduction yield, the MC-based geometrical acceptance factor, the energy-binned luminosity, and the corresponding solid angle, respectively. Here, Br indicates the branching fraction for the decay $\pi^0 \to \gamma\gamma$ (98.823%). The $F^i_{\rm bin}$ represents the correction factor for a binning effect, which arises from the mismatch of the 50 MeV-step division in the differential cross section measurement and the approximately 13 MeV-step digitization in the photon beam energy measurement by the tagging detector. Its variation depending on the energy bin is within a few %. The $F^i_{\rm conv}$ stands for the correction factor for the e^+e^- conversion rate of the final state γ's in the MC simulation, used to obtain A^i_{MC}. It is necessary because there is a slight discrepancy of the conversion rates in the real data and the simulated data due to the incomplete accuracy of the material inclusion in the MC simulation.

In Eq. (3), the efficiency for the proton detection at the BGOegg calorimeter or the DC is expressed by $\epsilon^i_{\rm proton}$. The proton detection efficiency of the DC has been discussed in Sec. III A. The corresponding quantity for the BGOegg calorimeter is identical with the efficiency of charge identification by the IPS. It was estimated by inspecting the real data sample where clean proton hits in the BGOegg calorimeter were collected without using the IPS. The individual proton detection efficiencies for the BGOegg calorimeter and the DC were combined to a single value of $\epsilon^i_{\rm proton}$ by taking the weighted average at the individual kinematical bins. The acceptance loss by the accidental DC hits due to e^+e^- pair creation at the liquid hydrogen target was also taken into account in the evaluation of $\epsilon^i_{\rm proton}$. This loss is reduced to 1–2 % thanks to the condition which allows additional charged tracks in the center part of DC, as described in Sec. III B.

The offline reconstruction efficiency of the tagging detector track [$\epsilon^i_{\rm tag}$ in Eq. (3)] was measured as a function of the photon beam energy. This efficiency also includes the detection efficiency of the scintillating fibers and the fraction of events where only one track is successfully selected at the reaction time. The photon beam energy was predicted by the kinematic fit of the reaction $\gamma p \to \pi^0\pi^0 p$ without the tagging detector information. The rate of finding a tagging detector track corresponding to the predicted photon beam energy was then calculated. The reconstruction efficiency varies from 88% to 93% depending on the photon energy.

The systematic errors of the differential cross section measurement were estimated at individual kinematical bins by considering the sources listed in Table I. The uncertainty of the energy-dependent transmission of the photon beam, described by Eq. (1), comes from variation of a fitting function and the normalization method. The former uncertainty was evaluated by replacing the second-order polynomial function to first- or third-order polynomials, which provides acceptable χ^2's as well. These functions were forced to pass the transmission correction factor of 1 in the highest beam energy region, where no beam loss is expected during the entire

TABLE I. Systematic error sources and their typical values for the differential cross sections in the present analysis. The error values are represented by the percentage to the differential cross sections at various kinematical bins.

Systematic error source	Typical error values
Energy-dependent transmission	
Fitting function variation	0.2–1.0 %
Normalization method	2.8%
Estimation by e^+e^- conversions	0.3–2.0 %
Photon beam position shift	0.1–7.7 %
Different χ^2 probability cut	0.3–2.1 %
Target length accuracy	1.3%
Br($\pi^0 \to \gamma\gamma$) error	0.034%

experimental period. The latter uncertainty was given by changing a sample used for the normalization at the highest beam energies. Instead of adopting the entire period, only the most reliable periods with no beam shift were conservatively used for making the normalization sample. Thus, the transmission correction factor of the highest energy bin can differ from 1 for the whole data sample, and this difference has been treated as a systematic uncertainty. In addition, the systematic error arising from how to estimate the energy dependence was obtained by an alternative method with e^+e^- conversion events, as described in Sec. II C. Among the systematic error sources related to the energy-dependent transmission, the uncertainty due to using different normalization methods turned out to be dominant.

A shift of the photon beam position also influences the geometrical acceptance measurement. Its systematic variation was evaluated by accepting a possible amount of the shift in the MC simulation. This error strongly varies depending on the kinematical bins. The present analysis applies the χ^2 probability cut at 2% after the kinematic fit. For quantifying the uncertainty depending on the cut position, the differential cross sections were recalculated by requiring the χ^2 probability to be greater than 10%, above which its distribution is ideally flat. This uncertainty was found to be about 2% or less. Another source of the systematic error arises from the accuracy of the target cell length. The target cell was made by thin films with dome shape surfaces at the forward and backward ends because of internal pressure. The uncertainty of the target length was estimated to be small by taking into account the photon beam spread and the beam position shift together with the cell shape. The branching fraction for the decay $\pi^0 \to \gamma\gamma$ possesses a measurement error, affecting the differential cross sections. According to the Particle Data Group (PDG) [22], the branching ratio error is negligibly small compared

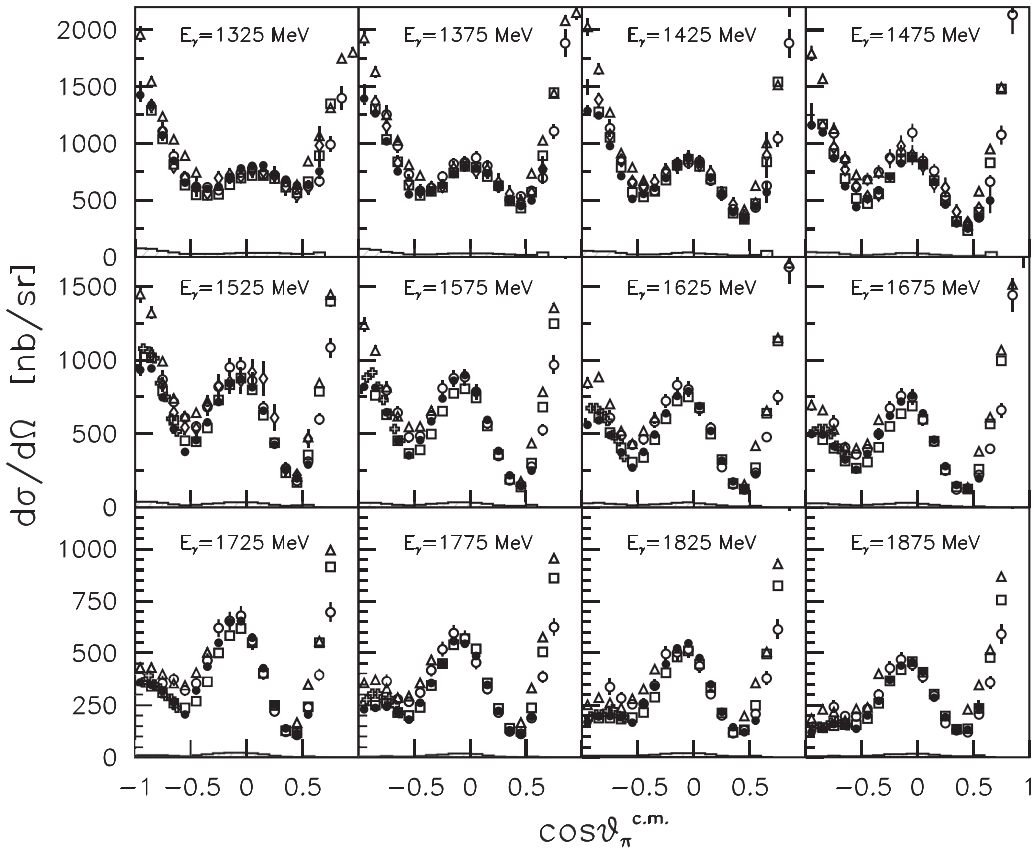

FIG. 5. Differential cross sections for $\gamma p \to \pi^0 p$ at the photon beam energies (E_γ) of 1300–1900 MeV. The present results from the BGOegg experiment are indicated by closed circles with statistical errors. The histograms show the systematic errors of the BGOegg measurement. The other data points come from the existing experimental results: CLAS (open square) [15], CB-ELSA (open circle) [10], CBELSA/TAPS (open triangle) [14], GRAAL (open diamond) [9], and LEPS Collaborations (open cross) [17].

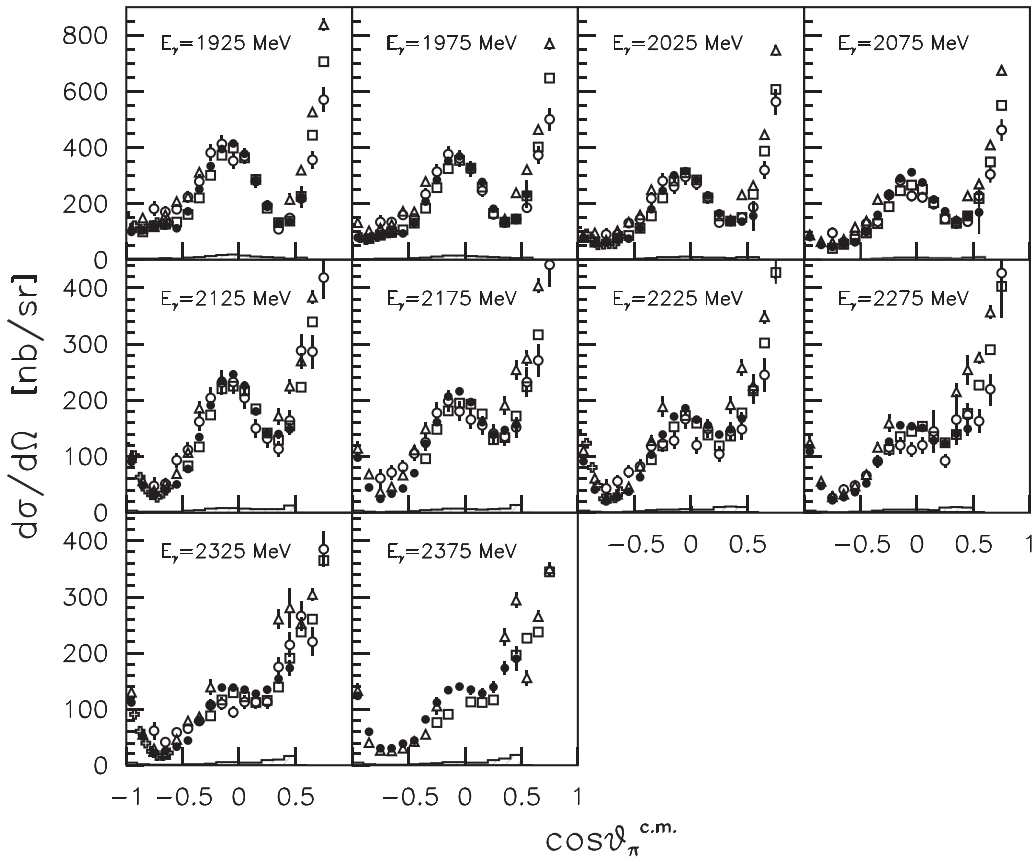

FIG. 6. Differential cross sections for $\gamma p \to \pi^0 p$ at the photon beam energies (E_γ) of 1900–2400 MeV. The present results from the BGOegg experiment are indicated by closed circles with statistical errors. The histograms show the systematic errors of the BGOegg measurement. The symbols for the other data points have the same meanings as in Fig. 5.

with the other systematic errors. The total systematic errors at individual kinematical bins were evaluated by taking the quadratic sum of the listed uncertainties. They vary in the range of 3–10 %, giving a typical value of 4% (5%) at the higher (lower) energies.

Figures 5 and 6 show the measured differential cross sections for the 22 photon beam energy ranges with 50 MeV steps. The present results by the BGOegg experiment are plotted by closed circles with statistical errors as a function of the π^0 polar angle with a 0.1 step in $\cos\theta_{\pi^0}^{\rm c.m.}$. In the present measurement, the statistical errors become relatively smaller at backward π^0 angles because of the larger geometrical acceptance. The overlaid histograms with a hatched pattern represent the systematic errors, described above.

The other symbols in the same figures denote the results available from the CLAS [15], CB-ELSA [10], CBELSA/TAPS [14], GRAAL [9], and LEPS [17] collaborations. The CLAS, CB-ELSA, and CBELSA/TAPS results have been obtained for the photon beam energy bins of each 50 MeV in the same way as the present analysis. There is only one exception with a 100 MeV width for $2300 < E_\gamma < 2400$ MeV in the CB-ELSA results, and the corresponding differential cross sections are plotted on the panel of $E_\gamma = 2325$ MeV in Fig. 6. The LEPS measurement has been carried out with 50 MeV bins at $1500 < E_\gamma < 2000$ MeV, while 100 MeV bins are used at $2000 < E_\gamma < 2400$ MeV. The LEPS data points above 2000 MeV are plotted on the panels of $E_\gamma = 2025$, 2125, 2225, and 2325 MeV in Fig. 6. The GRAAL differential cross sections have been derived with 20–28 MeV intervals at $E_\gamma < 1541$ MeV. In Fig. 5, these cross sections are plotted on the panels whose central energy value is closest to that of the GRAAL energy bin.

The BGOegg results provide high statistics data, comparable with the other experiments in the photon beam energy region of 1.3–2.4 GeV and a wide angle range, other than the very forward region of $\cos\theta_{\pi^0}^{\rm c.m.} > 0.7$. In contrast, the CLAS data do not cover the extremely backward angles especially at higher energies. The LEPS measurement add new data at the extremely backward angles. The CB-ELSA and CBELSA/TAPS results have been obtained by two complementary angle coverages in the detector setup and the trigger logic. Their individual polar angle ranges are rather limited. The GRAAL data are restricted to the lower energy region.

As seen in Figs. 5 and 6, every angular dependence of differential cross sections indicates a similar tendency among the plotted experimental results for each incident photon energy. In all the results, the differential cross sections generally decrease as the photon beam energy increases. In addition to the forward and backward enhancements, a bump distribution shows up in the intermediate angle range around $\cos\theta_{\pi^0}^{\rm c.m.} \approx 0$ at all the energies. This suggests that significant s-channel resonance contributions still dominate over the t-channel cross

sections in the energy range of $1300 < E_\gamma < 2400$ MeV. In the intermediate angle range, the differential cross sections of all the experiments agree with each other if their systematic errors are also considered. Thus we expect that there are no big problems on the normalization factors to evaluate the differential cross sections in those experiments. At backward angles, the differential cross sections of the present analysis are close to the results of CLAS, GRAAL, and LEPS. On the other hand, the differential cross sections of the CB-ELSA and CBELSA/TAPS measurements deviate from the present results more than the statistical and systematic errors especially at the lower energies. The ratios of their cross sections to the BGOegg values reach at most 1.5 in the most backward region. The differences become smaller at the higher energies.

Reference [15] by the CLAS collaboration has claimed that the measured differential cross section data can be explained only with the four-star resonances listed by PDG [22], e.g., $N(1535)S_{11}$, $N(1720)P_{13}$, $\Delta(1232)P_{33}$, $\Delta(1700)D_{33}$, as a result of their PWA. The present result by the BGOegg experiment, which shows good agreement with the CLAS measurement, can support this argument for the mass range below about 2 GeV/c^2.

Reference [10] by the CB-ELSA collaboration has mentioned the evidences of additional resonances including $N(1700)D_{13}$, N^*s of mass 2000 MeV/c^2 or more, and Δ^*s of mass above 1910 MeV/c^2, most of which are ranked with lower stars by PDG. Moreover, Ref. [14] has found the importance of $N(2070)D_{15}$, $N(2080)D_{13}$, and $N(2190)G_{17}$ with the χ^2 minima in the PWA which uses the differential cross sections measured at higher energies by the CBELSA/TAPS experiment. The $N(2190)G_{17}$ is rated as a four-star state by PDG, while the others are not listed. It would be difficult to advance rigorous discussions about the contributions of higher resonances, whose masses exceed about 2 GeV/c^2, only by referring to the differential cross sections because of their relatively weak appearance on the cross sections. The data of spin observables like the photon beam asymmetries must help the clarification at higher energies with the enhancement of smaller signals by interference.

B. Photon beam asymmetry

In addition to the differential cross sections, the photon beam asymmetries Σ were measured in 16 energy bins for $1300 < E_\gamma < 2400$ MeV and 16 polar angle bins for $-1.0 < \cos\theta_{\pi^0}^{\rm c.m.} < 0.6$. For the event selection to extract the photon beam asymmetries, an additional condition was introduced by limiting a proton detection area at the DC to the circular region with the radius of 600 mm. This condition was imposed to avoid making an artificial asymmetry due to the hexagonal DC shape.

At the individual kinematical bins of the photon beam energy and π^0 polar angle, the number of $\gamma p \to \pi^0 p$ events were counted after dividing the signal sample further into eight bins on the π^0 azimuthal angle relative to the linear polarization vector of the photon beam. Since our geometrical acceptance has rotational symmetry around the photon beam axis, no acceptance correction is applied when the azimuthal angle dependence of the π^0 photoproduction is measured.

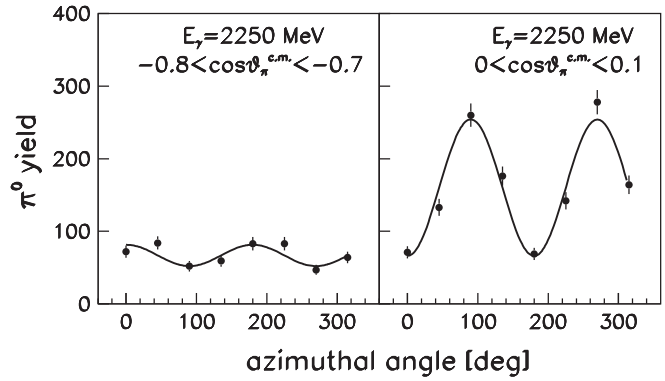

FIG. 7. Modulation of the measured $\gamma p \to \pi^0 p$ signal yield as a function of the azimuthal angle of the reaction plane relative to the photon beam polarization vector. Two cases of the π^0 polar angle ranges are shown for $2200 < E_\gamma < 2300$ MeV.

A possible systematic error due to the small imperfection of the rotational symmetry in the acceptance was examined by comparing the two data sets collected with vertically and horizontally polarized photon beams. The magnitudes of π^0 yield modulation in the azimuthal direction were found to be statistically consistent with each other between those two data sets in all the kinematical bins. Therefore, the vertical and horizontal polarization data samples were added after adjusting the polarization vector directions to 0°. We observe clear modulation patterns such as the examples shown in Fig. 7.

The obtained modulation patterns of the π^0 photoproduction yield $N(\phi)$ were fitted by the following equation:

$$N(\phi) = A(1 - \Sigma' \cos 2\phi), \tag{4}$$

where ϕ represents the azimuthal angle of the π^0 emission or the reaction plane relative to the photon beam polarization vector. The absolute value of Σ' denotes the magnitude of the azimuthal asymmetry. The positive (negative) sign of Σ' means that the reaction plane is more aligned to the direction perpendicular (parallel) to the polarization vector. The photon beam asymmetry Σ was finally obtained by correcting Σ' with the degree of photon beam polarization. The beam polarization was derived as described in Sec. II A together with a further correction due to the polarization of the injected laser light. The degree of laser polarization was typically 98%.

The systematic errors for the photon beam asymmetries were estimated as summarized in Table II. As discussed above, the differences of photon beam asymmetries between

TABLE II. Systematic error sources and their typical values for the photon beam asymmetries in the present analysis. The magnitudes of uncertainties in Σ's have been evaluated at various kinematical bins.

Systematic error source	Typical error values
Difference of two polarization data	0.003–0.04
Another binning of azimuthal angle	0.002–0.02
Ambiguity of polarization vector	0.001–0.008
Accuracy of laser polarization degree	0.04% of $\lvert\Sigma\rvert$

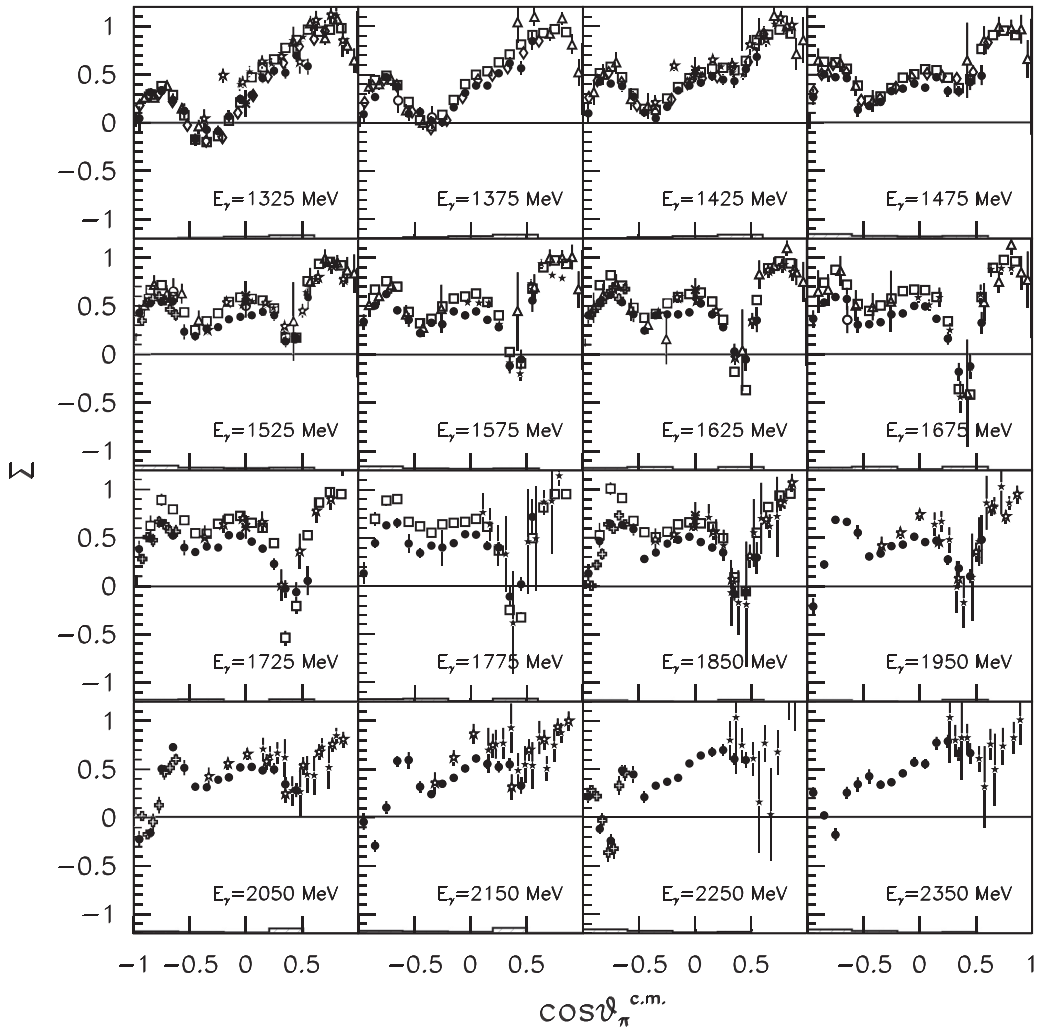

FIG. 8. Photon beam asymmetries for $\gamma p \to \pi^0 p$ at the photon beam energies (E_γ) of 1300–2400 MeV as a function of $\cos\theta_{\pi^0}^{\rm c.m.}$. The present results from the BGOegg experiment are indicated by closed circles with statistical errors. The histograms show the systematic errors of the BGOegg measurement. The other data points come from the existing experimental results: CLAS (open square) [16], CBELSA/TAPS (open triangle) [13], GRAAL (open diamond) [9], LEPS (open cross) [17], Daresbury (closed and open stars) [5,6], CEA (asterisk) [3], and Yerevan Collaborations (open circle) [4].

the two data sets with the vertically and horizontally polarized beams are small, but they are conservatively treated as systematic errors. The influence of statistical fluctuation has been removed in this comparison by combining about ten kinematical bins. The evaluated uncertainties are comparable or smaller than the statistical errors. Another source of the systematic error may come from the limited number of bins for the azimuthal angle. This error was estimated with a different binning method, where the ranges of eight azimuthal bins were shifted by 22.5°. In the comparison of the two binning methods at combined kinematical bins, their differences in Σ's are not large.

The polarization vector of the photon beam was used as the reference angle of the photon beam asymmetry. They were determined based on the polarization measurement for the injected laser light. Because there may be rotational ambiguity between the laser optical system and the BGOegg detector frame, a possible systematic error was estimated by retaking the reference angles of the vertical and horizontal polarization data from the individual modulation patterns of the reaction plane in the detector coordinate itself. This effect turned out to be small. The uncertainty in the degree of laser polarization, calculated by averaging many measurements, is negligible compared with the other systematic errors. As a result of taking the quadratic sum of the described uncertainties, the total systematic errors in Σ's are in the range of 0.006–0.050 depending on the kinematical bins.

Figure 8 shows the measured photon beam asymmetries Σ as a function of the π^0 polar angle, which is binned in each 0.1 of $\cos\theta_{\pi^0}^{\rm c.m.}$. The data points obtained by the present analysis are indicated by closed circles with statistical error bars. The photon beam energy ranges of individual panels have been arranged to 50 and 100 MeV for $1300 < E_\gamma < 1800$ and $1800 < E_\gamma < 2400$ MeV, respectively, because of statistics. The systematic errors for the present results are shown by histograms in each panel.

In addition to the BGOegg results, the existing photon beam asymmetries measured by other experiments are overlaid in the corresponding panels for comparison. These data are from the CLAS [16], CBELSA/TAPS [13], GRAAL [9], LEPS [17], Daresbury [5,6], CEA [3], and Yerevan Collaborations [4]. The energy bin widths of them completely differ from each other: 17–36 MeV for CLAS, 25 or 27 MeV for GRAAL, 33 MeV for CBELSA/TAPS, 100 or 200 MeV for LEPS, 80 MeV for Daresbury (1976), 100 MeV for Daresbury (1979), 100 MeV for CEA, and 150 MeV for Yerevan. Basically the data points other than the present results are plotted in the corresponding panel, so that the central value of its energy range (the displayed energy) is closest to the mean value of the energy bin in the individual measurements. If this mean energy accords with the boundary of the energy bins in Fig. 8 (e.g., the 100 MeV width of the LEPS measurement and the 50 MeV bin in the present analysis), the panel in the lower energy side is chosen to plot the data point.

The upper bounds of the photon beam energy ranges for the photon beam asymmetry measurement are 1500, 1680, and 1862 MeV in the GRAAL, CB-ELSA, and CLAS experiments, respectively, while their acceptances in terms of the π^0 polar angle range are rather wide including its forward photoproduction. The LEPS experiment has provided the asymmetry data in the photon beam energy range of 1500–2400 MeV but only in the backward region of $\cos\theta_{\pi^0}^{\mathrm{c.m.}} < -0.6$ with a limited acceptance. The measurements at CEA, Yerevan, and Daresbury were carried out in 1970s. The two Daresbury results have covered the photon beam energy region above 1.9 GeV, but the π^0 polar angle range is restricted to a forward region with large statistical errors. The present analysis for the BGOegg experiment provides the photon beam asymmetries in a wide kinematical region, corresponding to the photon beam energy range of 1300–2400 MeV and the π^0 polar angle range of $-1 < \cos\theta_{\pi^0}^{\mathrm{c.m.}} < 0.6$. Although the forward acceptance is moderate, the precise measurement over a wide angular range is given here for the first time at the higher energy region above 1.9 GeV.

Most of the experimental measurements show the $\cos\theta_{\pi^0}^{\mathrm{c.m.}}$ dependence similar to each other in all the energy ranges, although a variation of the measured absolute values is seen at the photon beam energies around 1.5–1.9 GeV. The present results are consistent with the LEPS results, whereas their absolute values are systematically smaller than the CLAS results. This difference is larger than the estimated systematic uncertainty, and the reason is as yet unknown.

The measured photon beam asymmetries are positive at most of the inspected kinematical bins. In the π^0 polar angle dependence, the asymmetry values drop symmetrically at $\cos\theta_{\pi^0}^{\mathrm{c.m.}} \approx \pm 0.6$ for a wide energy range. This behavior

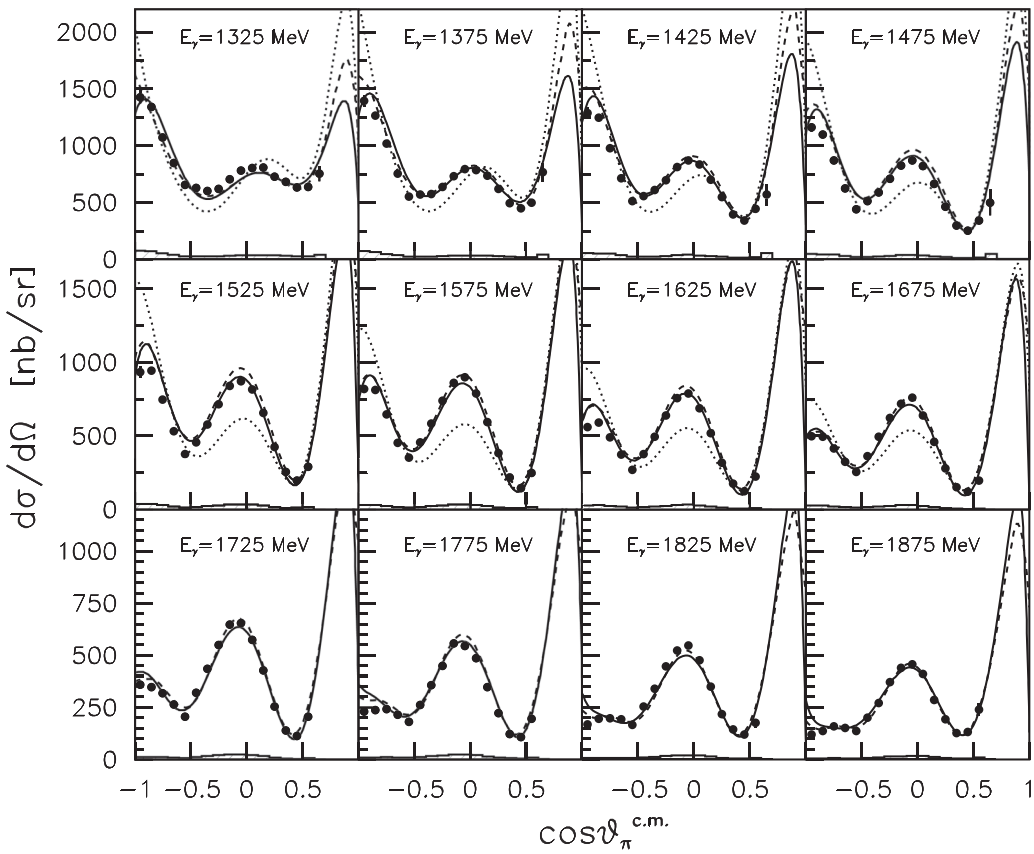

FIG. 9. Comparison of the existing PWA results and the present results (closed circle) for the differential cross sections at $1300 < E_\gamma < 1900$ MeV. The solid, dashed, and dotted curves show the PWA model calculations by the Bonn-Gatchina [31], SAID [32], and ANL-Osaka Collaborations [33], respectively. The histograms show the systematic errors of the BGOegg measurement.

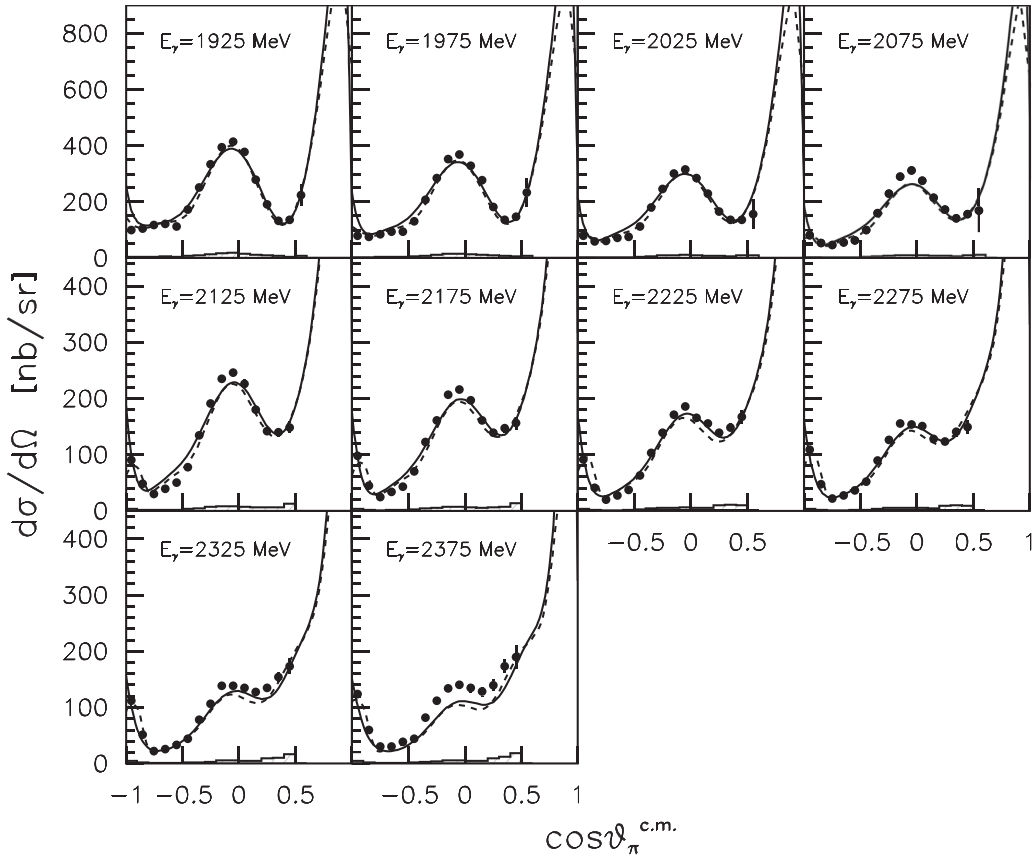

FIG. 10. Comparison of the existing PWA results and the present results (closed circle) for the differential cross sections at $1900 < E_\gamma < 2400$ MeV. The meanings of the individual lines and the histograms are the same as in Fig. 9.

indicates the interference of multipole amplitudes with various orbital angular momenta, as argued in Ref. [16]. The polar angle dependence including the magnitudes of the dip structures strongly varies as a function of the photon beam energy, suggesting the continuous change of individual amplitude contributions. As the photon beam energy exceeds 1.9 GeV, a drop of the photon beam asymmetry becomes prominent at the most backward angles. In the highest energy region, a significant drop of the asymmetry is apparent at $\cos\theta_{\pi^0}^{\rm c.m.} \approx -0.75$. This point is discussed later in Sec. V. Because photon beam asymmetry data over a wide polar angle range were lacking in the higher energy region, our new results are important for partial wave analyses of baryon resonances.

V. DISCUSSIONS

In order to extract baryon resonances from the mass spectrum, a PWA is necessary with the input of measured differential cross sections and spin observables. Several groups (e.g., Bonn-Gatchina [26], SAID [27], MAID [28], ANL-Osaka [29], Jülich-Bonn Collaborations [30]) have constructed the frameworks of PWA, which simultaneously fit theoretical curves to the experimental observables obtained from the πN scattering and the meson photoproduction of π, η, K, etc. We compare our results with the existing PWA calculations below.

Figures 9 and 10 show the comparison of the measured differential cross sections and the PWA model curves calculated by the Bonn-Gatchina (BG2014-02) [31], SAID (Chew-Mandelstam fit CM12) [32], and ANL-Osaka Collaborations (the 2016 model) [33]. Since the differential cross section data for the reaction $\gamma p \to \pi^0 p$ have been available from many other experiments, the existing PWA calculations generally agree with our results. The model calculations by Bonn-Gatchina and SAID are mostly consistent with each other. Small inconsistencies at backward angles are within a variation of the differential cross sections measured by different experiments. The PWA results by the ANL-Osaka group are available only in the lower energy region because higher mass channels like ωN are not included yet.

Figure 11 shows the photon beam asymmetries calculated by the existing PWA models. The present results are also plotted in the same figure. At the lower energies, the PWA calculations are more or less consistent with the experimental data. The differences among the PWA models increase above $E_\gamma \approx 1.6$ GeV at forward π^0 angles. In the higher energy region above 1.9 GeV, where the experimental data becomes scarce, none of the PWA models reproduce the measured photon beam asymmetries. The Bonn-Gatchina results largely deviate from the measured values at the most backward angles, while they reproduce the data points at $\cos\theta_{\pi^0}^{\rm c.m.} > -0.6$. In contrast, the SAID calculation has successfully expressed the dip structure of the photon beam asymmetries at

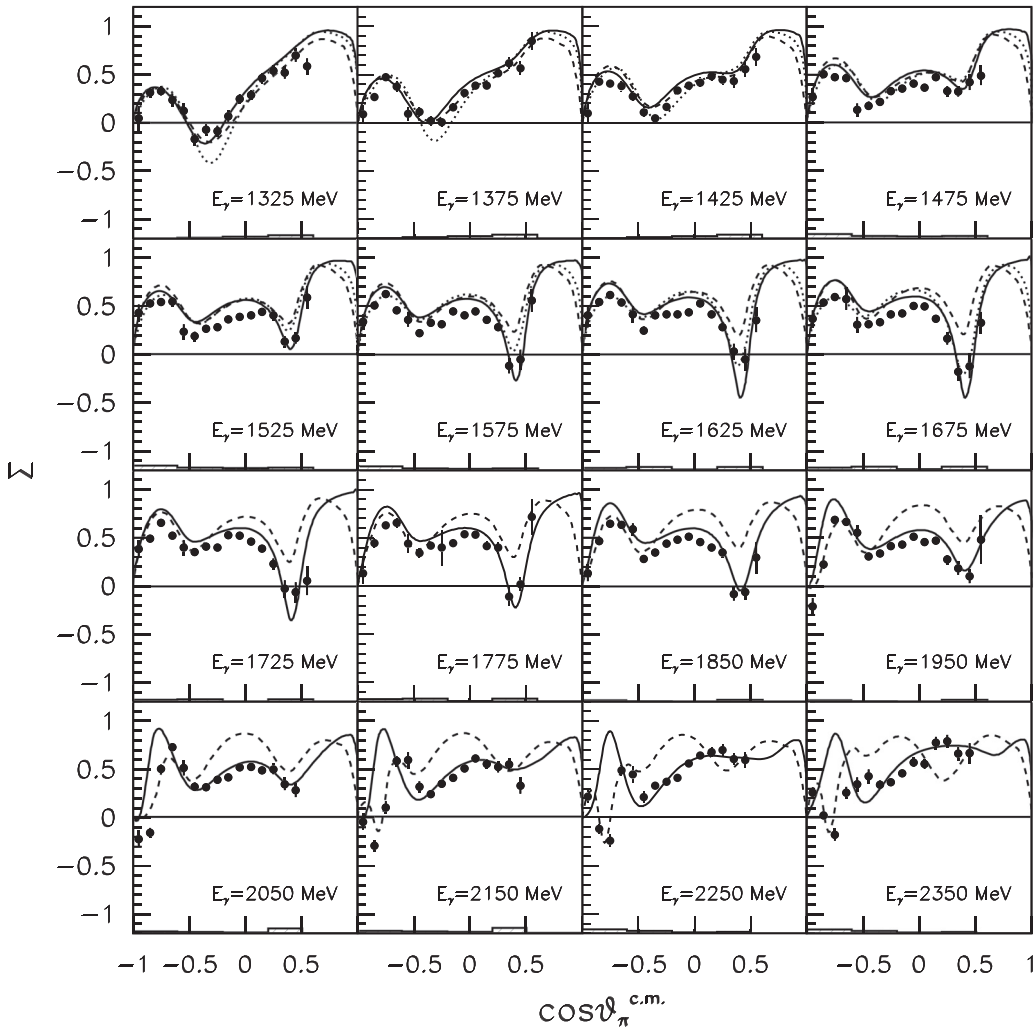

FIG. 11. Comparison of the existing PWA results and the present results (closed circle) for the photon beam asymmetries at $1300 < E_\gamma < 2400$ MeV. The solid, dashed, and dotted curves show the PWA model calculations by Bonn-Gatchina [31], SAID [32], and ANL-Osaka Collaborations [33], respectively. The histograms show the systematic errors of the BGOegg measurement.

$\cos\theta_{\pi^0}^{\text{c.m.}} < -0.7$ by utilizing the LEPS backward results in their PWA fit. However, the SAID results do not agree with our new experimental data at $-0.5 < \cos\theta_{\pi^0}^{\text{c.m.}} < 0.5$.

In order to recognize the source of deviations between the PWA results in the high energy region, we have examined the multipole amplitudes, from which the information about the partial waves of the meson-nucleon system can be extracted. (See Table 2 of Ref. [34] for the reference of their correspondence.) For the photoproduction of pseudoscalar mesons, the multipole amplitudes are used to construct four components of the so-called Chew-Goldberger-Low-Nambu (CGLN) amplitudes [35] in the form of linear combinations of Legendre polynomials [18]. The CGLN amplitudes can be further translated to the four helicity amplitudes, whose combination formulates the unpolarized differential cross section σ_0 and photon beam asymmetry Σ as follows [18,36]:

$$\sigma_0 = \frac{1}{2}\frac{q}{k}(|H_1|^2 + |H_2|^2 + |H_3|^2 + |H_4|^2), \tag{5}$$

$$\Sigma = \frac{q}{k}\frac{1}{\sigma_0} Re(H_1 H_4^* - H_2 H_3^*), \tag{6}$$

where H_i $(i = 1, 2, 3, 4)$ are the helicity amplitudes corresponding to the different spin flip transitions. The q and k represent the magnitudes of three-momenta for the pion and photon, respectively, in the center-of-mass system. Since the multipole amplitudes are openly available from all the PWA models, the above observables have been calculated for comparisons by changing the multipole amplitudes step by step.

Figure 12 shows the SAID PWA calculation results for the differential cross section and photon beam asymmetry in higher energy regions ($E_\gamma = 2225$ and 2250 MeV, respectively). The experimental data points are overlaid in the same figures. As explained above, the dip structure of the measured photon beam asymmetry at $\cos\theta_{\pi^0}^{\text{c.m.}} \approx -0.75$ is well fitted by the SAID model calculation, which includes the multipole amplitudes corresponding to the orbital angular momenta of a πN system (L) from 0 up to 5. This calculation also agrees with the measured differential cross sections. However, the backward dip structure of the photon beam asymmetry by the SAID calculation vanishes when the inclusion of multipole amplitudes are restricted to $0 \leqslant L \leqslant 4$. The disappearance

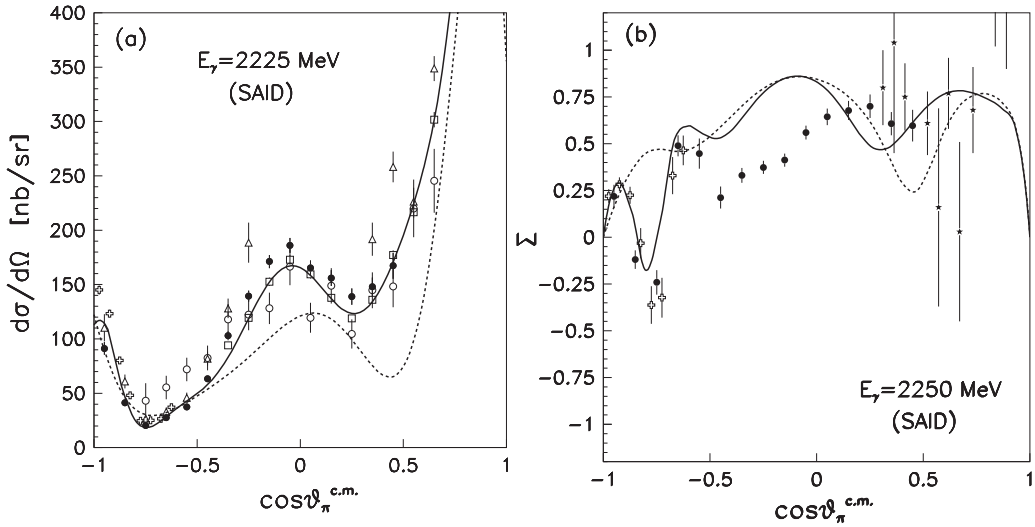

FIG. 12. The existing SAID calculation results of (a) differential cross section and (b) photon beam asymmetry with the orbital angular momenta of a πN system up to 5 (solid line) and 4 (dashed line) in high energy regions: 2200–2250 MeV for the differential cross section and 2200–2300 MeV for the photon beam asymmetry. The symbols in (a) and (b) represent the experimental results shown in Figs. 6 and 8.

of interference is most apparent in the case of removing the M_{5-} multipole, whose quantum number is the same as the πN partial waves of H_{19} and H_{39} with $J^P = \frac{9}{2}^+$. This suggests the importance of a high spin resonance state at higher energies. The PDG [22] has listed the $N(2220)H_{19}$ and $\Delta(2300)H_{39}$ as four-star and two-star states, respectively, in the corresponding mass region.

A similar analysis of multipole amplitudes has been also performed for the Bonn-Gatchina model calculation, as shown in Fig. 13. The analyzed energy ranges and the experimental data points in Fig. 13 are the same as those in Fig. 12. For both the differential cross section and photon beam asymmetry, the calculated results are mostly unchanged even by lowering the maximum L contribution from 9 to 4. The photon beam asymmetry of the Bonn-Gatchina model calculation with $0 \leqslant L \leqslant 4$ is significantly different from the corresponding curve of the SAID calculation. This suggests a large ambiguity in the amplitude solutions up to $L = 4$ at the photon beam energies above 1.9 GeV.

Figure 14 shows the SAID and Bonn-Gatchina model calculations with various ranges of L in a lower energy region ($E_\gamma = 1625$ MeV). In both models, the calculated results of the differential cross section and photon beam asymmetry are converged by adopting the multipole amplitudes up to $L = 3$. In addition, they approximately reproduce the experimental results. This indicates that the multipole amplitudes have fewer ambiguities at lower energies, as expected from the existence of many measurements.

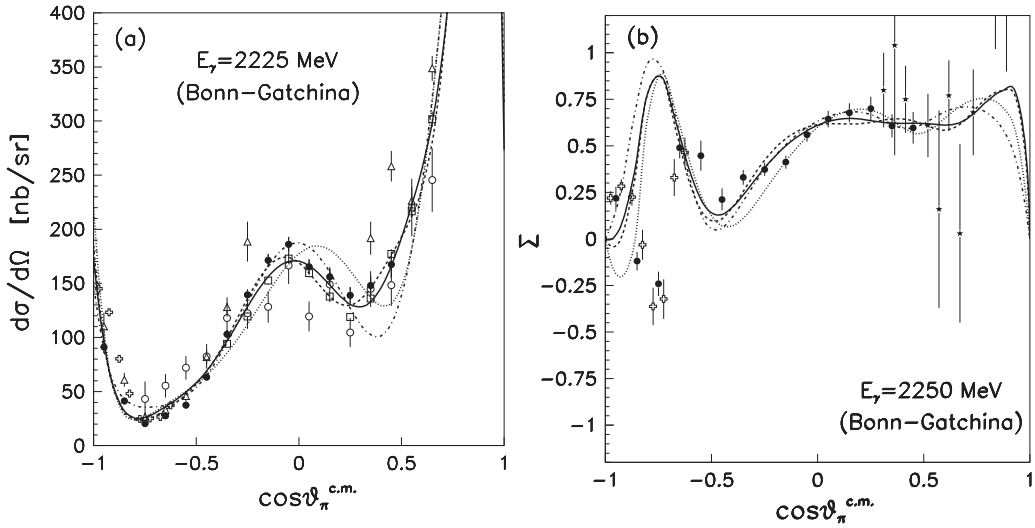

FIG. 13. The existing Bonn-Gatchina calculation results of (a) differential cross section and (b) photon beam asymmetry with the orbital angular momenta of a πN system up to 9 (solid line), 7 (dashed line), 5 (dotted line), and 4 (dash-dotted line) in the high energy regions, same as in Fig. 12. The experimental results indicated by symbols are also the same as those in Fig. 12.

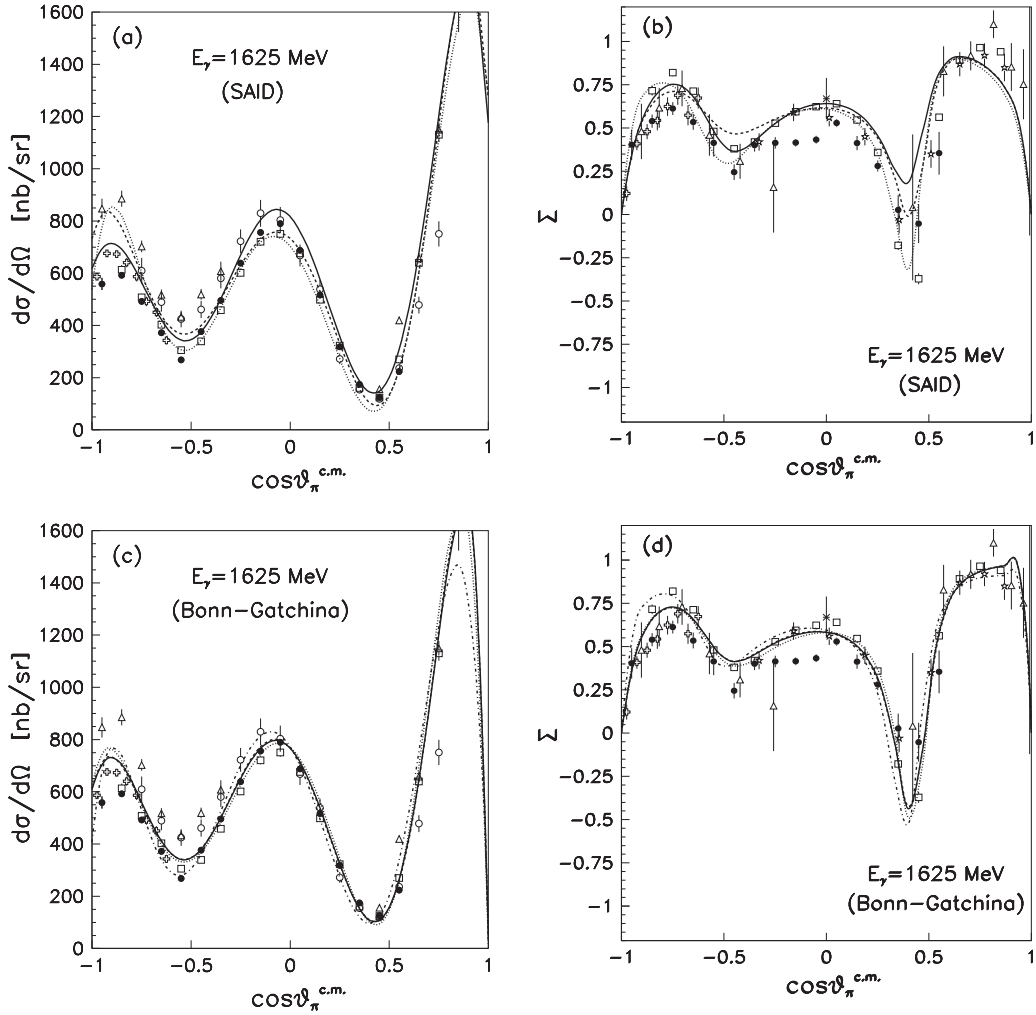

FIG. 14. The existing PWA calculation results of differential cross sections [(a) and (c)] and photon beam asymmetries [(b) and (d)] in a low energy region (1600–1650 MeV). (a) and (b) show the SAID results with the orbital angular momenta of a πN system L up to 5 (solid line), 4 (dashed line), and 3 (dotted line). (c) and (d) display the Bonn-Gatchina curves with $L \leqslant 9$ (solid line), $L \leqslant 7$ (dashed line), $L \leqslant 5$ (dotted line), and $L \leqslant 3$ (dash-dotted line). The experimental results are simultaneously plotted with the same symbols as in Figs. 5 and 8.

VI. SUMMARY

The BGOegg experiment has been running at the LEPS2 beamline of SPring-8, where the tagged photon beam of 1.3–2.4 GeV is produced by laser Compton scattering. This photon beam is linearly polarized, and the degree of polarization reaches more than 90% at the Compton edge. We have employed a large-acceptance electromagnetic calorimeter BGOegg equipped with charged particle detectors to study single π^0 photoproduction off the proton. The π^0 decaying into $\gamma\gamma$ was measured by the BGOegg calorimeter providing the world-best energy resolution, whereas a recoil proton was detected in the larger acceptance range including both the BGOegg calorimeter and the forward planar DC for the determination of its flying direction. A kinematic fit was performed to select the signals of the reaction $\gamma p \to \pi^0 p$ without hardly any background contamination. A wide π^0 polar angle range, except for the forward region, was examined to measure the differential cross sections and the photon beam asymmetries.

The differential cross sections have been derived with the high statistical precision comparable to other experimental results. The typical systematic errors are reduced to 4–5% with various efficiency corrections. The $\cos\theta_{\pi^0}^{\mathrm{c.m.}}$ dependence with a bump structure at intermediate angles indicates the importance of s-channel resonance contributions. The measured differential cross sections are consistent with the results from the CLAS, GRAAL, and LEPS experiments. On the other hand, the CB-ELSA and CBELSA/TAPS data deviate from the present results at the backward π^0 angles in the photon beam energy region below 1.9 GeV. Our new result will help to constrain the strengths of the resonance couplings. The differential cross sections modeled by several PWA groups more or less agree with our measured data. However, the solutions for the multipole amplitudes are converged only at the lower energies below about 1.9 GeV. Small resonance contributions with a higher mass and spin can be unambiguously investigated by combining the spin observables with the differential cross sections.

The π^0 polar angle dependence of the measured photon beam asymmetries Σ continuously varies as a function of the photon beam energy. The dip structures from the positive asymmetry to smaller values are observed at $\cos\theta^{\rm c.m.}_{\pi^0} \approx \pm 0.6$, indicating the interference caused by the multipole amplitudes with higher orbital angular momenta. The polar angle and energy dependences of the measured photon beam asymmetries are very similar to those of the existing experimental results from CLAS, CBELSA/TAPS, GRAAL, LEPS, etc., below the photon beam energy around 1.9 GeV. There is at most several tens of % variation in the magnitudes of asymmetries among the different experiments. The present results are consistent with the earlier LEPS measurement. In the high energy region above 1.9 GeV, the present analysis provides the unprecedented information of Σ with high precision over a wide π^0 polar angle range. A new dip structure appears at $\cos\theta^{\rm c.m.}_{\pi^0} \approx -0.75$, and a multipole amplitude analysis suggests the contribution from the orbital angular momentum of 5 in a πN system. The observed $\cos\theta^{\rm c.m.}_{\pi^0}$ dependence is not reproduced by the existing PWA model calculations. The amplitude solutions by PWA models are still uncertain at high energies, and the new input by the present analysis will refine our understanding of high mass resonance states.

ACKNOWLEDGMENTS

The authors greatly acknowledge to the support of the staff at SPring-8 for helping the commissioning of the LEPS2 beamline and providing the excellent experimental conditions during the data collection. We thank T. Sato, A. Sarantsev, and V. Nikonov for discussions on the theoretical issues. This research was supported in part by the Ministry of Education, Culture, Sports, Science and Technology of Japan, JSPS KAKENHI Grant No. 24244022, Scientific Research on Innovative Areas Grant No. 21105003, Grant-in-Aid for Specially Promoted Research Grant No. 19002003, and the Ministry of Science and Technology of Taiwan.

[1] E. Klempt and J.-M. Richard, Rev. Mod. Phys. **82**, 1095 (2010).
[2] S. Capstick and W. Roberts, Prog. Part. Nucl. Phys. **45**, S241 (2000).
[3] J. Alspector *et al.*, Phys. Rev. Lett. **28**, 1403 (1972).
[4] L. O. Abrahamian *et al.*, Phys. Lett. B **48**, 463 (1974).
[5] P. J. Bussey *et al.*, Nucl. Phys. B **104**, 253 (1976).
[6] P. J. Bussey *et al.*, Nucl. Phys. B **154**, 492 (1979).
[7] R. Beck, Eur. Phys. J. A **28**, Suppl. 1, 173 (2006).
[8] P. Adlarson *et al.*, Phys. Rev. C **92**, 024617 (2015).
[9] O. Bartalini *et al.*, Eur. Phys. J. A **26**, 399 (2005).
[10] O. Bartholomy *et al.*, Phys. Rev. Lett. **94**, 012003 (2005).
[11] H. van Pee *et al.*, Eur. Phys. J. A **31**, 61 (2007).
[12] D. Elsner *et al.*, Eur. Phys. J. A **39**, 373 (2009).
[13] N. Sparks *et al.*, Phys. Rev. C **81**, 065210 (2010).
[14] V. Crede *et al.*, Phys. Rev. C **84**, 055203 (2011).
[15] M. Dugger *et al.*, Phys. Rev. C **76**, 025211 (2007).
[16] M. Dugger *et al.*, Phys. Rev. C **88**, 065203 (2013).
[17] M. Sumihama *et al.*, Phys. Lett. B **657**, 32 (2007).
[18] R. L. Workman *et al.*, Eur. Phys. J. A **47**, 143 (2011).
[19] N. Muramatsu *et al.*, Nucl. Instrum. Methods Phys. Res. A **737**, 184 (2014).
[20] A. D'Angelo *et al.*, Nucl. Instrum. Methods Phys. Res. A **455**, 1 (2000).
[21] S. Agostinelli *et al.*, Nucl. Instrum. Methods Phys. Res. A **506**, 250 (2003); J. Allison *et al.*, IEEE Trans. Nucl. Sci. **53**, 270 (2006).
[22] M. Tanabashi *et al.* (Particle Data Group), Phys. Rev. D **98**, 030001 (2018).
[23] T. Ishikawa *et al.*, Nucl. Instrum. Methods Phys. Res. A **837**, 109 (2016).
[24] http://www.spring8.or.jp/en/users/operation_status/schedule/bunch_mode.
[25] M. J. Berger *et al.*, NIST Standard Reference Database 8, available at https://www.nist.gov/pml/xcom-photon-cross-sections-database.
[26] A. V. Anisovich *et al.*, Eur. Phys. J. A **24**, 111 (2005); A. V. Anisovich and A. V. Sarantsev, *ibid.* **30**, 427 (2006); A. V. Anisovich *et al.*, *ibid.* **44**, 203 (2010).
[27] R. L. Workman, M. W. Paris, W. J. Briscoe, and I. I. Strakovsky, Phys. Rev. C **86**, 015202 (2012).
[28] D. Drechsel *et al.*, Nucl. Phys. A **645**, 145 (1999); Eur. Phys. J. A **34**, 69 (2007).
[29] H. Kamano, S. X. Nakamura, T. S. H. Lee, and T. Sato, Phys. Rev. C **88**, 035209 (2013); **94**, 015201 (2016).
[30] D. Rönchen *et al.*, Eur. Phys. J. A **50**, 101 (2014); **51**, 70 (2015).
[31] https://pwa.hiskp.uni-bonn.de/.
[32] http://gwdac.phys.gwu.edu/.
[33] T. Sato (private communication).
[34] A. V. Anisovich *et al.*, Eur. Phys. J. A **52**, 284 (2016).
[35] G. F. Chew, M. L. Goldberger, F. E. Low, and Y. Nambu, Phys. Rev. **106**, 1345 (1957).
[36] R. L. Walker, Phys. Rev. **182**, 1729 (1969).